Mesoscale phase distribution in single particles of LiFePO$_4$ following lithium deintercalation

Ulrike Boesenberg[1,a], **Florian Meirer**[2], **Yijin Liu**[3], **Alpesh K. Shukla**[1], **Rossana Dell'Anna**[2], **Tolek Tyliszczak**[4], **Guoying Chen**[1], **Joy C. Andrews**[3], **Thomas J. Richardson**[1], **Robert Kostecki**[1], and **Jordi Cabana**[1,*]

[1]Environmental Energy Technologies Division, Lawrence Berkeley National Laboratory, 1 Cyclotron Rd., Berkeley, CA 94720

[2]Fondazione Bruno Kessler, Center for Materials and Microsystems, Via Sommarive 18, I-38050 Povo, Trento, Italy

[3]Stanford Synchrotron Radiation Lightsource, SLAC National Accelerator Laboratory, 2575 Sand Hill Road, Menlo Park, CA 94025 (USA)

[4]Advanced Light Source, Lawrence Berkeley National Laboratory, Berkeley, California 94720, 20036, USA

Abstract

The chemical phase distribution in hydrothermally grown micrometric single crystals LiFePO$_4$ following partial chemical delithiation was investigated. Full field and scanning X-ray microscopy were combined with X-ray absorption spectroscopy at the Fe K- and O K-edges, respectively, to produce maps with high chemical and spatial resolution. The resulting information was compared to morphological insight into the mechanics of the transformation by scanning transmission electron microscopy. This study revealed the interplay at the mesocale between microstructure and phase distribution during the redox process, as morphological defects were found to kinetically determine the progress of the reaction. Lithium deintercalation was also found to induce severe mechanical damage in the crystals, presumably due to the lattice mismatch between LiFePO$_4$ and FePO$_4$. Our results lead to the conclusion that rational design of intercalation-based electrode materials, such as LiFePO$_4$, with optimized utilization and life requires the tailoring of particles that minimize kinetic barriers and mechanical strain. Coupling TXM-XANES with TEM can provide unique insight into the behavior of electrode materials during operation, at scales spanning from nanoparticles to ensembles and complex architectures.

[*]Corresponding author: jcabana@lbl.gov.
[a]Present address: HASYLAB at DESY, Notkestr. 85, D-22607 Hamburg, Germany

Supporting Information Available: Electron diffraction data of delithiated crystals; expanded data analysis of FFTXM data in the paper; additional TXM-XANES images of different areas in the samples analyzed in this study. This material is available free of charge via the Internet at http://pubs.acs.org.

Keywords

intercalation reactions; chemical imaging; battery electrode materials; $LiFePO_4$

Introduction

Lithium ion batteries operate through the redox (de)insertion of lithium into (from) electroactive host materials.[1–3] The ability of the materials to accommodate the chemical phase transformations that accompany the variations in lithium concentration determines electrode utilization and cycle life. In turn, these phase transformations are determined by the crystal and electronic structure of the compound, for instance by controlling the pathways that charge carriers can follow in and out of a crystal. Particle size and morphology can lead to kinetic barriers that modify the reaction mechanism and its rate.[4,5] Thus, observation of phase transformations in single particles can provide insight that can be used in the design of materials with maximized performance.

$LiFePO_4$ is a canonical example of the importance of phase transformations in battery electrodes. It is converted to $FePO_4$ *via* a first-order phase transition at about 3.4 V vs. Li^+/Li^0.[6] The poor electrochemical utilization and cycling performance found in early reports was ascribed to the low ionic and electronic conductivity of the two compounds.[7] This limitation was subsequently overcome by engineering small primary particles with an electron conductive coating (typically, carbon),[8,9] to the point that fast rates and high utilization are now commonplace.[10,11] $LiFePO_4$ crystallizes in an olivine-type structure (*Pnma* space group) with Li^+ ions located in 1D channels along the *b* direction.[12] Although the crystal framework remains the same upon Li extraction, there are significant and anisotropic changes in the lattice parameters. A contraction in the 100 and 010 directions of 4.9 % and 3.5 %, respectively, is concomitant with an expansion of 1.9 % in the 001 direction. The lattice misfit leads to elastic deformation and thus coherency strain at the phase boundaries. The strain is anisotropic and could be minimized with appropriate control of particle morphology.[13] Another means for strain alleviation would be through the formation of solid solution phases with intermediate lithium contents, and, hence, cell dimensions. Their existence and role during the two-phase transformation is an active topic of discussion.[14–16] Nonetheless, it is now well established that as crystallite size decreases, the miscibility gap between the end members shrinks, thereby leading to decreased lattice strain.[17,18] Further, Malik *et al.*[19] and Bai *et al.*[20] recently proposed that, below a critical particle size, nucleation and phase growth within a single particle could be bypassed when applying an electrochemical overpotential, thereby enabling a single-phase transformation over the whole compositional range.

Several mechanisms have been proposed for the delithiation of $LiFePO_4$ to $FePO_4$ within a crystalline particle. The core-shell model initially proposed by Padhi *et al.*[21] was invalidated by the fact that the most favorable lithium diffusion path is through tunnels aligned with the *b* axis.[7,22,23] Chen *et al.*[14] observed the formation of narrow $FePO_4$ domains, stretched along the *c* direction in micron scale, hexagonal plate crystals of Li_xFePO_4 (where *x* is the overall lithium content in the sample). They proposed that these domains propagate along the *a* direction as the delithiation proceeds. Similar phase distributions were found in smaller crystals.[24,25] A "domino cascade" model of mesoscale transformation in nanoparticles was put forth by Delmas et al.,[26] in which, once nucleation of the new phase (e.g. $FePO_4$ in $LiFePO_4$) occurs, spontaneous and rapid transformation of the whole crystal takes place. As a result, at any given compositional point, all particles in an electrode are single phase, either $FePO_4$ or $LiFePO_4$. The means by which particles would communicate with one another to achieve this intricate sequential mechanism is not clear. Multiple studies have

been carried out to clarify this behavior, with results both supporting[26–28] as well as invalidating[4,25] the model. The striking inhomogeneity of charge (phase) distribution in LiFePO$_4$ electrodes may contribute to the experimental confusion.[29]

The number of more or less conflicting mechanisms underscores the experimental challenge of reliably visualizing the phase distribution in a single particle with high spatial (nm-range) *and* chemical resolution. Lithium contents in a material can be inferred from diffraction experiments,[26,30] or by measuring the local oxidation state of the redox center (e.g., Fe in LiFePO$_4$), using tools such as X-ray absorption spectroscopy (XAS)[31,32] or electron energy loss spectroscopy (EELS).[24,27] The latter can be combined with transmission electron microscopy (TEM) to produce chemical maps with the highest resolution possible today. However, TEM-EELS faces issues regarding sample preparation and stability, as LiFePO$_4$ and FePO$_4$ are known to be sensitive to decomposition under intense electron irradiation[33–35]. The fact that only thin sections of particles in limited fields of view (FOV~1 μm) can be successfully analyzed by TEM-EELS also raises the question of how representative the observations are of the entire sample. In contrast, virtually all the X-ray or neutron-based tools used to characterize battery materials so far produce results averaged over a large volume of sample. Recently, spatial resolutions of 20 nm and below have been achieved by transmission X-ray microscopy (TXM).[36] TXM can be performed in scanning (STXM) and full field (FF TXM) mode. The main conceptual difference is in the means to achieve spatial resolution, either through beam focusing (STXM) or image formation with an objective lens (FF TXM).[37] Both tools enable a FOV of several microns within minutes, even seconds. When using a tunable synchrotron source for the measurement, simultaneous collection of XAS is possible without sacrificing spatial resolution. Further, penetration through tens of micrometers of matter can easily be achieved with hard X-rays. This feature enables the performance of experiments during an electrochemical reaction (*in operando*), as recently demonstrated in 2D mode, albeit without simultaneous XAS collection.[38,39] Despite an early 3D FF TXM study at the Mo K-edge with a resolution of about 2–3μm,[40] the field of chemically resolved TXM has been dominated by STXM in the soft X-ray region.[41–44] More recently, FF TXM has been applied to distinguish chemical compositions at the Ni K[45] and Ti L-edges.[46] The latter report showed that hard X-ray TXM is particularly suited to the study of hierarchical structures in functional materials such as battery electrodes due to the strong X-ray penetration and depth of focus, enabling the study of large areas in 2D and 3D.[47–49]

Here, STXM and FF TXM in combination with X-ray absorption near edge spectroscopy (XANES) for nanoscale imaging of phase transformations are applied to produce high chemical and spatial resolution maps for partially delithiated, micron-sized LiFePO$_4$ crystals. Regions of both LiFePO$_4$ and FePO$_4$ were thus resolved. Their mesoscale distribution was analyzed vis-à-vis the mechanism of phase transformation and the microstructure of the crystals, which was revealed by complementary electron microscopy experiments.

Experimental

Sample preparation and definition

LiFePO$_4$ crystals measuring ca. $2 \times 0.2 \times 4$ μm along the *a, b*, and *c* axes, respectively, were synthesized using a previously described hydrothermal method.[14] Partially delithiated samples were prepared by stirring the crystals in a 0.05 M solution of bromine in acetonitrile in a specific molar ratio corresponding to the desired lithium content. Powder X-ray diffraction patterns were obtained using a Phillips X'Pert diffractometer with an X'celerator detector and Cu Kα radiation. The average composition of the delithiated batches was determined by Rietveld refinement.

Electron microscopy

Scanning electron microscopy (SEM) was performed in a JEOL 7500F operated at 1 kV and 20μA in gentle beam mode. For transmission electron microscopy, crystals were dispersed on an ultra-thin carbon supported grid and studied in a Zeiss Libra microscope operating at 200 kV using zero-loss energy filtered, selected area electron diffraction (SAED) and bright field imaging in conventional TEM (CTEM) mode, and high-angle annular dark field (HAADF) imaging in scanning TEM (STEM) mode. The electron diffraction patterns were also simulated using Single Crystal software.[50] The smallest available condenser (C2) aperture (1.5 microns) was used to probe areas close to the edge of the crystal. This resulted in a parallel illumination of an area approx. 40 nm in diameter on the sample. This method was used instead of selected area diffraction and convergent beam electron diffraction in order to select a smaller area and also minimize radiation damage from the electron beam.

Transmission X-ray microscopy

2D STXM- and FF TXM-XANES were collected from pristine $LiFePO_4$ and from partially and fully delithiated crystals. For the measurements, crystals were sprinkled directly on Si_3N_4 membranes (Silson Inc.) of 200 nm thickness for FF TXM and on 20 nm carbon coated Cu TEM grids (Ted Pella, Inc.) for STXM. STXM was performed at beamline 5.3.2.1 at the Advanced Light Source (ALS), Lawrence Berkeley National Laboratory, using an interferometer-controlled stage. The instrumental setup is described in detail in the literature.[51] Two dimensional mapping was performed at selected energies in the vicinity of the O-K-edge (520–570 eV) with a spatial resolution of 25 nm. For all data processing, aXis2000 software[52] was used.

Full field (FF) TXM was performed at the wiggler beamline 6–2 at the Stanford Synchrotron Radiation Lightsource (SSRL), SLAC National Accelerator Laboratory.[53] The microscope is optimized for photon energies in the range of 5 to 14 keV with spatial and energy resolutions of 30 nm and $\Delta E/E = 10^{-4}$, respectively, and achieves a single flat field of view (FOV) of about 20×20 μm. 2D XANES images (0.5 sec. exposure time, 50 repetitions, binning 2) were collected from 7080 to 7260 eV in 74 steps at varying energy intervals, with spectral sampling at 1 eV in the immediate Fe K-edge region. This approach was followed to maximize energy resolution at the energies where the main features were expected (e.g., the white line and the first oscillations that follow) while optimizing measurement time by collecting fewer points above and below these features. Nonetheless, these points are important for XANES normalization, and therefore covered a wide energy range: about 100 eV above and 50 eV below the white line. The zone plate was adjusted at each energy to maintain focus. To account for changes in flux and small beam instabilities, a set of reference images was recorded at each energy (0.5 s exposure time, 40 repetitions, binning 2) in regions where the transmission of the beam was unobstructed by the sample, and subsequently subtracted from the FOV of interest. The XANES measurement for a single FOV was accomplished in 1.5h.

FF TXM data analysis

A single FOV in FF TXM-XANES consisted of 1024×1024 pixels (p) collected at 74 energies (E), generating a data matrix $p \times E$. Principal component analysis (PCA) was used to reduce the dimensionality of this 74 dimensional data space, while preserving the relevant information, by describing the data in a way which best explains the variance of the entire data set.[54,55] PCA produces principal components (PCs) which are linear combinations of the E independent variables and sorts them in descending order according to the level of variance associated with each PC. These PCs generally cannot be interpreted as the spectra of individual chemical phases, but rather provide an orthogonal basis set that optimally describes the data in terms of its variance. As a result, the data can be represented by a new

matrix, $p \times PC_{1..E}$, where the PCs (columns) are eigenimages, while the rows represent eigenspectra. The PCs were determined by singular value decomposition (SVD) of the data matrix. Because SVD involves the calculation of a matrix $p \times p$, which is in our case too large for computer memory, the "economy size" decomposition of the data matrix was used.[56,57] The dimensionality of the data matrix $p \times PC_{1..E}$ was then reduced to $p \times PC_{1..N}$ without losing significant information by choosing the first N principal components that explain most of the data variance ("cumulative variance explained", or CVE). Because PCs are oriented to best describe the spread in the data, projecting the latter to the N-dimensional PC space (score plot) highlights the pattern explained by the captured variance and effectively reduces noise, which is now described by PCs having indices larger than N. The distance between data points in the score plot is a direct measure of the similarity of the XANES, i.e. the chemical phase. Therefore, k-means clustering[58,59] of the data points in the reduced PC space was performed, grouping pixels according to their (Euclidean) distances from cluster centers (centroid linkage method). As a result, pixels with similar XANES were effectively clustered into k groups. Because the PCs form an orthogonal basis set, each of the N PCs describes an uncorrelated spread of the data cloud. For this reason, PCA indicates that there are at least N different groups of XANES, i.e. at least N different chemical identities present in the data. Therefore, the number of clusters k has to be at least equal to N in order to exploit all the information provided by the reduced PC space. The different chemical identities identified by PCA do not necessarily directly correspond to actual pure chemical phases, but are represented by irreducible XANES within the data set. As a consequence, the number of real chemical phases is necessarily still at least N. Comparison with spectra of known standards was subsequently used to match the irreducible spectra produced by PCA with chemical phases (or combinations thereof).

The single pixel XANES spectra of a single FOV containing several crystals in the pure $LiFePO_4$ and $FePO_4$ samples were averaged to produce reference spectra. These standards were used for the identification of chemical phases after PCA, and for the linear combination (LC) fitting of all the single pixel XANES spectra in a single FOV for the partially delithiated samples. Errors were calculated following the approach of the FEFFIT program,[60] as described in the program documentation.[61] All data processing, including reference correction, averaging, magnification correction, XANES reconstruction and fitting, was performed using the TXM-Wizard software.[62]

Results

STEM HAADF imaging of pristine $LiFePO_4$ crystals revealed a number of dark spots and streaks (Figure 1a). Intensity in a HAADF STEM image is related exponentially to the mass thickness and is roughly proportional to the square of the average atomic number. Therefore, assuming that there is no variation in composition within a crystal, this contrast can be attributed to its mass thickness. These dark features were ascribed to microstructural defects such as cracks or voids. A high defect density was found in the center of the crystal, in contrast to the dense and defect-free outer edges, which appear more uniform. The SEM image of similar pristine crystals in Figure 1b shows only the surface morphology. The density of defects was much lower, indicating that they were mostly buried within the bulk of the particles. Only a few cracks were present, oriented roughly along the c-direction. Careful SAED analysis did not reveal visible misorientations within a single particle (Figure S1). A notable increase in the number of cracks and grooves was induced in the crystals by delithiation, as exemplified in Figures 1c and d for samples with a nominal composition of $Li_{0.5}FePO_4$. The surface features observed by SEM were straight, parallel to the c axis and evenly spaced (Figure 1d). The STEM image in Figure 1c shows that internal fracture lines also developed. In some cases, they were found to extend across both the dense edges and defective center, but, overall, their density appeared to be lower in the former. Analysis of

the phase distribution was attempted by coupling STEM with electron energy loss spectroscopy (EELS). However, the crystal thickness (about 200 nm) resulted in significant plural scattering that made the analysis unreliable, thus providing motivation for our TXM-XANES study.

The normalized Fe K edge XANES transmission spectra for single-phase $LiFePO_4$ and $FePO_4$ obtained in FF TXM mode (Figure 2) show a significant edge shift of about 2 eV upon oxidation from Fe^{2+} ($LiFePO_4$) to Fe^{3+} ($FePO_4$), along with a decrease in the whiteline intensity and shifting of post-edge features to higher energies. The calculated transmission for the 200 nm thick platelets at these high energies was about 95% and, therefore, the corresponding signal was near the lower detection limit. Two sets of crystals with bulk composition $Li_{0.74}FePO_4$ and $Li_{0.5}FePO_4$, as determined from refinements of powder XRD data, were studied by FF TXM-XANES. The transmission image collected at 7080 eV from the first sample (Figure 3a) shows a large platelet with two smaller superimposed crystal fragments. As in STEM imaging, decreased brightness contrast in this transmission image corresponds to areas with lower mass density, in this case, due to macroscopic defects. Principal component analysis (PCA) and subsequent k-means clustering were performed following the approach described by Lerotic *et al.*[63] to identify the number of Fe-containing species and their distribution within the sample. The number of PCs capturing the relevant information of the dataset was determined graphically by plotting the CVE (scree plot) and by inspecting the eigenimages and eigenspectra. In our case, the first two PCs captured an overall variance of 99.2% (Figure S2). The linear spread of the data cloud in the reduced space spanned by the first 2 PCs (score plot, Figure 4a) clearly showed the existence of a linear phase transition between two groups of most different chemical identities, i.e. different XANES. In order to explore this linear phase transition we intentionally over-clustered ($k > N$) the data cloud using $k = 5$ (arbitrary value). The FF TXM-XANES image was consequently segmented into 5 clusters of pixels (Figure 4b) having similar XANES. The average spectra of clusters 4 and 5 (cyan and purple in Figure 4a) represented the two most different chemical identities in the sample. They were in excellent agreement with the spectra collected for $LiFePO_4$ and $FePO_4$ standards, respectively (Figures 4a), the end members of the phase transformation. Further, the comparison of the average XANES of each of the 5 clusters (Figure 4c) identified the regions where different extents of transformation occurred, following the order, from $LiFePO_4$ to $FePO_4$: cluster 4, cluster 2, cluster 1, cluster 3, cluster 5. Thus, without using any *a priori* knowledge of the actual chemistry of the sample, PCA and *k*-means clustering of the FF TXM-XANES dataset: i) proved that all XANES in the map were a linear combination of two and only two chemical phases unambiguously identified as $LiFePO_4$ and $FePO_4$ and ii) allowed an image segmentation displaying the spatial distribution of the two phases.

Based on the PCA results, the XANES spectrum of each pixel was fitted by a linear combination of the two standards ($LiFePO_4$, $FePO_4$) to obtain a two dimensional phase-map as an RGB image (Figure 3b). Green and red colors indicate pure $LiFePO_4$ and $FePO_4$, respectively, whereas the blue color is purest for pixels with a 1:1 $LiFePO_4$:$FePO_4$ ratio. Representative XANES spectra for two selected single pixels and the corresponding LC fits are presented in Figure 5. The phase fractions for the single pixels have an accuracy of about 5 %. Single pixels showing poor signal-to-noise ratios due to low Fe concentration were filtered out by setting their intensity to 0 at all energies.[45,62] Therefore, they appear black in the chemical maps. Averaging all the single pixel compositions in the map gave a particle composition, Li_xFePO_4, with $x = 0.85 \pm 0.03$, somewhat higher than the nominal sample composition. Because slight spatial misalignments of the image stack may lead to incorrect assignment of phases due to intensity variations, especially at particle edges, randomly selected pixels were examined to verify their signal-to-noise ratios, and agreement between phase assignments and edge position. No edge effects were observed in this data set. The

phase distribution determined by LC fitting of the single pixel XANES (Figure 3b) agreed well with the phase distribution determined from the PCA cluster distribution (Figure 4b). In both cases, regions of extensive delithiation appeared at edge locations, while the center of the crystal was mostly unchanged. Nonetheless, some pixels with non-negligible amounts of $FePO_4$ were found in the center of the crystals and $LiFePO_4$ rich sites were also detected at the edges in the two maps. Since the transmission mode spectra represent an average over the thickness (ca. 200 nm) of the crystal, mixed compositions most likely resulted from incomplete delithiation in the b direction, i.e., $FePO_4$ was located mostly at the surface of the crystals when mixed contents were present. In another crystal from the same sample (Figure S3), with a slightly lower lithium content (x = 0.8 ±0.04), larger $FePO_4$ domains were found at the edge sites, while much less delithiation, albeit still non-negligible, was observed in the center.

The effect of extensive delithiation was analyzed in the sample with $Li_{0.5}FePO_4$ nominal composition. The transmission image at 7080 eV of a selected field of view containing a collection of crystals (Figure 6a) shows one large platelet lying flat, with multiple smaller ones with different orientations above or below. Cracks along the length of the large crystal (c-direction) together with contrast between center and edge regions were observed, consistent with the STEM images. PCA and k-means clustering of this field of view (Figures S4 and S5) confirmed the extensive delithiation of the crystal: comparison with reference XANES shows that the two most different XANES found are $FePO_4$ (clusters 4 and 1, at the edges of the crystal) and a mixture of the latter and a small amount of $LiFePO_4$ (clusters 5 and 3, in the center of the crystal). The overall local composition in this specific field of view was approximately Li_xFePO_4 with x=0.06, indicating that kinetic factors during the chemical reaction determine the ultimate phase ratio in the individual crystals. The phase distribution map obtained by LC fitting (Figure 6b) shows extensive delithiation both at the edges and in the defective interior. Correlation between microstructure and chemical composition was observed. The boundary between delithiated and lithiated regions at the edges formed a pattern that appeared to follow the original outline of the dense edges vs. the more defective inner region. The pixels with highest $FePO_4$ contents in the center were found to be more randomly located than those along the edges. However, evidence of $FePO_4$ elongated domains in the c direction that bear some correlation to the distribution of cracks in the center of the crystal were found, as shown in insets I and II in Figure 6b (see also Figure S6). The spatial resolution in the experiment did not allow us to clearly determine whether delithiated domains existed along the crack, as opposed to right next to it, as suggested by Chen et al.[14] Finally, a few crystals were aligned vertically in the beam and showed a cross section suggesting a sandwich structure with delithiation dominantly at the (010) surfaces. This pattern would be consistent with only partial delithiation along the b axis due to interruption by defects. However, the number of pixels across the depth of the particle was too small, so that a definite conclusion could not be reached. Crystals from the $Li_{0.5}FePO_4$ sample varied considerably in composition, further highlighting the inhomogeneity of the reaction. In one with x = 0.57 ±0.04 (Figure S7), delithiation along the crystal edges was incomplete. Here, delithiation was extensive in the center, with some apparent c-elongated domains visible in the bottom half of the crystal.

Similar analysis of mesoscale phase distribution was carried out on different crystals in the same sample (nominal composition $Li_{0.5}FePO_4$) by STXM-XANES at the O-K edge. The corresponding spectra of single-phase $LiFePO_4$ and $FePO_4$ (Figure 7a) were obtained by accumulating signals during line scans across the particles. Both spectra showed a pre-edge feature at ca. 532 eV, followed by a pronounced jump. In contrast with FF TXM, the particles investigated here were near the upper thickness limit of the tool. Indeed, the low energies used in these experiments resulted in much higher absorption of photons by the crystals than using hard X-rays. As a result, the intensity observed above 538 eV and at the

Fe L_{III} edge (not shown) was too low and, consequently, the features too distorted to perform a reliable chemical phase analysis. Nonetheless, the intensity of the O K pre-edge absorption feature was much higher for $FePO_4$ than for $LiFePO_4$, in agreement with previous reports.[24,31] This intensity is related to increased polarization of the O^{2-} ions by Fe^{3+} vs. Fe^{2+}, which results in stronger hybridization of the Fe-O orbitals. Therefore, chemical contrast between the two states could be achieved by collecting images at energy corresponding to this resonance. The image collected at 528 eV, below any absorption threshold (Figure 7b), shows only mass thickness contrast. The darker areas in the center of the crystals indicate regions of lower density relative to the denser (lighter) edges. Multiple dark spots were observed in the center region of the crystal, which are assigned to defects such as voids or cavities. The image in Figure 7c was obtained at 532.8 eV, which corresponds to the maximum of the pre-edge peak (Figure 7a). Hence, it contains information on both the density and the chemical phase distribution. The lightest areas, such as the edges of the crystals, had the highest content of $FePO_4$. The image in Figure 7d was obtained by normalization of image c to image b, and shows enhanced chemical contrast (Figure 7d). Here, the dark regions correspond to those richest in $FePO_4$. The results were largely consistent with FF TXM-XANES, with the edges showing more extensive delithiation and notable compositional inhomogeneities among them (see examples in Figure S8).

Discussion

The pristine $LiFePO_4$ platelet-like crystals contain holes and cracks localized mainly in their center, the edges being denser and more homogeneous. Comparison of SEM and STEM data, which probe different depths, revealed that these macroscopic imperfections preferentially accumulated inside the particles (Figures 1a and b). Their formation is dependent on the crystal growth process and the synthesis conditions. Lu *et al.* grew $LiFePO_4$ crystals in a range of particle sizes and shapes up to several micrometers by a similar hydrothermal method.[64] They observed ring-like structures for intermediate reaction times in the presence of ammonia and citric acid. The centers of these particles appeared to be defective and redissolved during the growth process. Another possible origin for the defects in the present crystals is that purging with argon gas was performed as part of the synthesis procedure to prevent iron oxidation.[14] Some gas may have been trapped in the solid, causing either internal voids or defects. In some cases, the gas could be released upon prolonged heating in the hydrothermal vessel, leading to defects that propagate to the surface (Figure 1b). The edges are less defective because less gas was trapped there.

Delithiation of the $LiFePO_4$ platelets was found to be more favorable at crystal edge locations than in the center of the crystals. Since lithium can only be removed from $LiFePO_4$ along the *b* direction,[65] which corresponds to the thickness of the plate, this peculiar behavior cannot be explained by a thermodynamic control of the delithiation of a single crystal. Instead, it appears to be dominated by the microstructural features of the particles. The presence of objects with a variety of defect numbers and arrangements would be consistent with inhomogeneous delithiation within the same batch, as observed especially in the $Li_{0.5}FePO_4$ (nominal composition) sample. An additional effect could be the deviation from equilibrium of the chemical delithiation reaction caused by inefficient contact between the oxidizing agent and the particles when immersed in the reaction medium and stirred. The tendency for the denser areas of the crystals, which are the edges in the present case, to be more fully delithiated is consistent with the requirement of a contiguous diffusion path for lithium ions to reach the crystal surface. Such contiguous path does not exist in the presence of internal cracks and voids. The oxidizing solution cannot reach the unreacted areas through the solid surface, whereas the absence of material prevents solid state diffusion. Thus, it is likely that the surface in the center of crystals may have started delithiating at the

same time as the edges, but the reaction was interrupted in the presence of voids and cracks, while it could proceed continuously in defect-free areas. Comparison of the phase distribution with the morphological information collected by STEM provided evidence of partial delithiation in both the edges and center of the crystals, for instance, in Figures 3, S3 and S8. It also revealed that the delithiated outer regions always included the edge of the crystal. Given the 1D character of Li diffusion within the $LiFePO_4$ framework, crystal edges and corners cannot be considered, a priori, as more favorable points of reaction than domains within the crystal. Non-random distribution of atomic-level defects[65] and/or local gradients of strain could influence these results, but could not be properly evaluated in this study. At any rate, modeling of the initiation of the phase transformation in the presence and absence of a particle edge[66,67] would be beneficial to explain these results. Higher spatial resolution would also be required to discern the exact orientation of the $LiFePO_4$/$FePO_4$ boundaries. While the global pattern does not follow either the *a* or *c* directions, it could well be that local sub-domains do, and that the progress of the reaction is kinetically controlled even in these dense regions, resulting in a complex pattern. Indeed, staggered phase boundaries along the [101] direction were reported in earlier TEM observations.[25] In contrast to the complex orientation of the delithiated domains on the edges, evidence was found that the corresponding domains in the center had a tendency toward anisotropy in the form of more or less subtle stripe patterns of delithiated phase, as indicated by the arrows in Figure 6. These stripes are highly reminiscent of the pattern reported by Chen *et al.* based on TEM imaging, and would thus be in agreement with their proposed delithiation mechanism in which an extended phase boundary preferentially forms along the *c* direction.[14]

The initial microstructure of the sample also determined the mechanical consequences of delithiation. Both EM and TXM images of partially delithiated samples revealed more severe cracking than in the pristine crystals. As fresh cracks develop at the surface during delithiation, pathways for penetration of the oxidizing solution to the interior are created, which likely facilitate more extensive delithiation.[35] Propagation of redox phase transformations along cracks was also reported to enable the electrochemical conversion of large NiO particles to Ni by Li, as revealed by 3D FF TXM-XANES.[45] The origin of the cracks was not fully revealed in our experiments. At the surface, they could be driven by the strain introduced by the lattice misfit between $LiFePO_4$ and $FePO_4$. The misfit is negative along the *a* and *b* directions, the former being largest, whereas it is small and positive along *c*.[68] In the presence of strong bonding between $LiFePO_4$ and $FePO_4$ domains, tensile stress will lead to cracking along the *c* direction in the delithiated phase, consistent with the observations in Figures 1c and d. A subtly different mechanism must operate in the interior, especially in view of the less extensive cracking observed in the dense areas around the edges. It would appear that the preexisting defects lead to higher brittleness in the center compared to the edge of the crystal. These areas cannot absorb the stress that accompanies delithiation, resulting in mechanical failure. In contrast, the dense edges must be more mechanically stable. Given that these domain sizes were as high as 200 nm along the *a* direction, it is possible that the critical size for mechanical failure upon extensive cycling does not impose the need for very small particles (below 100 nm)[69] for suitable electrode performance.

Conclusions

This study has revealed the interplay at the mesoscale between microstructure, mechanics and phase transformation in $LiFePO_4$ through the combination of nanoscale morphological and chemical imaging. TXM coupled with XANES was employed to produce chemical composition maps of micron-sized single crystals at different delithiation stages both with high spatial (30 nm) and chemical resolution. High accuracy was ensured by a robust data analysis procedure using PCA and k-means clustering. The correlation between STEM and

TXM-XANES imaging revealed complex behavior, proposed to result from a combination of kinetic and thermodynamic limitations. Thermodynamically, the transition is limited by the 1D character of the Li mobility within the material. STEM revealed macroscopic defects, possibly induced by the synthesis process, which dominated the kinetics of the phase transition within the crystals. Stresses accompanying the delithiation process led to mechanical failure along the c-axis, particularly in the defective center of the crystals, the dense edges remaining more intact. While mechanical failure and its correlation with the phase transformation are well established in electrode systems with colossal volume changes,[70] they are often overlooked in intercalation-based materials.[71] Further, the importance of microstructure in battery electrode operation is typically associated with carrier diffusion lengths. Our results stress the role of microstructure as a kinetic factor during transformation of a particle between the initial and the final state, especially when defects are considered. Many methods used nowadays for the synthesis of materials are designed to stabilize metastable morphologies, which, with few exceptions,[72] result in a high degree of microstructural complexity. Indirectly, our work implies that single particle studies directed at extracting fundamental conclusions using poorly designed and characterized materials are bound to produce misleading results. Finally, generally speaking, our results constitute further proof of the versatility of TXM-XANES, both in scanning and full field modes, especially when coupled with more widely available tools such as TEM, to pinpoint the origins of the behavior of electrode materials during operation. The wide tunability of the X-ray radiation provides high chemical sensitivity and opens the door to combined studies of materials and architectures at scales spanning from nanoparticles to ensembles and complex architectures such as those present in battery electrodes.

Supplementary Material

Refer to Web version on PubMed Central for supplementary material.

Acknowledgments

References

1. Goodenough JB, Kim Y. Chem. Mater. 2009; 22:587.

2. Whittingham MS. Chem. Rev. 2004; 104:4271. [PubMed: 15669156]

3. Park C-M, Kim J-H, Kim H, Sohn H-J. Chem. Soc. Rev. 2010; 39:3115. [PubMed: 20593097]

4. Wagemaker M, Mulder FM, Van der Ven A. Adv. Mater. 2009; 21:2703.

5. Belak AA, Wang Y, Van der Ven A. Chem. Mater. 2012; 24:2894.

6. Yamada A, Koizumi H, Nishimura S-i, Sonoyama N, Kanno R, Yonemura M, Nakamura T, Kobayashi Y. Nat. Mater. 2006; 5:357. [PubMed: 16617345]

7. Li J, Yao W, Martin S, Vaknin D. Solid State Ionics. 2008; 179:2016.

8. Ravet N, Chouinard Y, Magnan JF, Besner S, Gauthier M, Armand M. J. Power Sources. 2001:97–98. 503.

9. Zaghib K, Mauger A, Julien CM. J. Solid State Electrochem. 2012; 16:835.

10. Kang B, Ceder G. Nature. 2009; 458:190. [PubMed: 19279634]

11. Chong J, Xun S, Song X, Ridgway P, Liu G, Battaglia VS. J. Power Sources. 2012; 200:67.

12. Santoro RP, Newnham RE. Acta Cryst. 1967; 22:344.

13. Van der Ven A, Garikipati K, Kim S, Wagemaker M. J. Electrochem. Soc. 2009; 156:A949.

14. Chen G, Song X, Richardson TJ. Electrochem. Solid-State Lett. 2006; 9:A295.

15. Srinivasan V, Newman J. J. Electrochem. Soc. 2004; 151:A1517.

16. Gu L, Zhu C, Li H, Yu Y, Li C, Tsukimoto S, Maier J, Ikuhara Y. J. Am. Chem. Soc. 2011; 133:4661. [PubMed: 21391668]

17. Delacourt C, Poizot P, Tarascon J-M, Masquelier C. Nat. Mater. 2005; 4:254.

18. Meethong N, Huang HY, Carter WC, Chiang YM. Electrochem. Solid-State Lett. 2007; 10:A134.

19. Malik R, Zhou F, Ceder G. Nat. Mater. 2011; 10:587. [PubMed: 21765400]

20. Bai P, Cogswell DA, Bazant MZ. Nano Lett. 2011; 11:4890. [PubMed: 21985573]

21. Padhi AK, Nanjundaswamy KS, Goodenough JB. J. Electrochem. Soc. 1997; 144:1188.

22. Morgan D, Van der Ven A, Ceder G. Electrochem. Solid-State Lett. 2004; 7:A30.

23. Nishimura, S-i; Kobayashi, G.; Ohoyama, K.; Kanno, R.; Yashima, M.; Yamada, A. Nat. Mater. 2008; 7:707. [PubMed: 18690238]

24. Laffont L, Delacourt C, Gibot P, Wu MY, Kooyman P, Masquelier C, Tarascon JM. Chem. Mater. 2006; 18:5520.

25. Ramana CV, Mauger A, Gendron F, Julien CM, Zaghib K. J. Power Sources. 2009; 187:555.

26. Delmas C, Maccario M, Croguennec L, Le Cras F, Weill F. Nat. Mater. 2008; 7:665. [PubMed: 18641656]

27. Sigle W, Amin R, Weichert K, van Aken PA, Maier J. Electrochem. Solid-State Lett. 2009; 12:A151.

28. Brunetti G, Robert D, Bayle-Guillemaud P, Rouvière JL, Rauch EF, Martin JF, Colin JF, Bertin F, Cayron C. Chem. Mater. 2011; 23:4515.

29. Liu J, Kunz M, Chen K, Tamura N, Richardson TJ. J. Phys. Chem. Lett. 2010; 1:2120.

30. Chen G, Song XY, Richardson TJ. J. Electrochem. Soc. 2007; 154:A627.

31. Augustsson A, Zhuang GV, Butorin SM, Osorio-Guillen JM, Dong CL, Ahuja R, Chang CL, Ross PN, Nordgren J, Guo JH. J. Chem. Phys. 2005; 123:184717. [PubMed: 16292931]

32. Deb A, Bergmann U, Cramer SP, Cairns EJ. Electrochim. Acta. 2005; 50:5200.

33. Pan Y-H, Vaughan G, Brydson R, Bleloch A, Gass M, Sader K, Brown A. Ultramicroscopy. 2010; 110:1020.

34. Moreau P, Mauchamp V, Pailloux F, Boucher F. Appl. Phys. Lett. 2009; 94:123111.

35. Weichert K, Sigle W, van Aken PA, Jamnik J, Zhu C, Amin R, Acartürk T, Starke U, Maier J. J. Am. Chem. Soc. 2011; 134:2988. [PubMed: 22191608]

36. Falcone R, Jacobsen C, Kirz J, Marchesini S, Shapiro D, Spence J. Contemp. Phys. 2011; 52:293.

37. Grunwaldt J-D, Schroer CG. Chem. Soc. Rev. 2010; 39:4741. [PubMed: 20978666]

38. Nelson J, Misra S, Yang Y, Jackson A, Liu Y, Wang H, Dai H, Andrews JC, Cui Y, Toney MF. J. Am. Chem. Soc. 2012; 134:6337. [PubMed: 22432568]

39. Chao SC, Yen YC, Song YF, Sheu HS, C WH, Wu NL. J. Electrochem. Soc. 2011; 158:A1335.

40. Rau C, Somogyi A, Simionovici A. Nucl. Instrum. Methods Phys. Res. Sect. B. 2003; 200:444.

41. Graf-Zeiler B, Fink RH, Tzvetkov G. Chem. Phys. Chem. 2011; 12:3503. [PubMed: 21853515]

42. de Smit E, Swart I, Creemer JF, Hoveling GH, Gilles MK, Tyliszczak T, Kooyman PJ, Zandbergen HW, Morin C, Weckhuysen BM, de Groot FMF. Nature. 2008; 456:222. [PubMed: 19005551]

43. Warwick T, Franck K, Kortright JB, Meigs G, Moronne M, Myneni S, Rotenberg E, Seal S, Steele WF, Ade H, Garcia A, Cerasari S, Denlinger J, Hayakawa S, Hitchcock AP, Tyliszczak T, Kikuma J, Rightor EG, Shin HJ, Tonner BP. Rev. Sci. Instr. 1998; 69:2964.

44. Hitchcock AP, Dynes JJ, Johansson G, Wang J, Botton G. Micron. 2008; 39:311. [PubMed: 17996451]

45. Meirer F, Cabana J, Liu Y, Mehta A, Andrews JC, Pianetta P. J. Synch. Rad. 2011; 18:773.

46. Guttmann P, Bittencourt C, Rehbein S, Umek P, Ke X, Van Tendeloo G, Ewels CP, Schneider G. Nat. Photon. 2012; 6:25.

47. Shearing PR, Howard LE, Jørgensen PS, Brandon NP, Harris SJ. Electrochem. Commun. 2010; 12:374.

48. Chao S-C, Yen Y-C, Song Y-F, Chen Y-M, Wu H-C, Wu N-L. Electrochem. Commun. 2010; 12:234.

49. Gonzalez-Jimenez ID, Cats K, Davidian T, Ruitenbeek M, Meirer F, Liu Y, Nelson J, Andrews JC, Pianetta P, de Groot FMF, Weckhuysen BM. Angew. Chem. Int. Ed. 2012; 51:11986.

50. CrystalMaker®. Oxford, UK: CrystalMaker Software Ltd.; http://www.crystalmaker.com [Last accessed January 2013]

51. Kilcoyne ALD, Tyliszczak T, Steele WF, Fakra S, Hitchcock P, Franck K, Anderson E, Harteneck B, Rightor EG, Mitchell GE, Hitchcock AP, Yang L, Warwick T, Ade H. J. Synch. Rad. 2003; 10:125.

52. aXis 2000 - Analysis of X-ray Images and Spectra. Canada: McMaster University; http://unicorn.mcmaster.ca/aXis2000.html [Last accessed January 2013]

53. Andrews JC, Almeida E, van der Meulen MCH, Alwood JS, Lee C, Liu Y, Chen J, Meirer F, Feser M, Gelb J, Rudati J, Tkachuk A, Yun W, Pianetta P. Microsc. Microanal. 2010; 16:327. [PubMed: 20374681]

54. Joliffe, IT. Principal Component Analysis. 2nd ed.. New York: Springer; 2002.

55. Jackson, JE. A User's Guide to Principal Components. John Wiley & Sons, Inc.; 2003.

56. G. H. Golub, GH.; Van Loan, CF. Matrix Computations. 3rd ed.. Baltimore, MD: The Johns Hopkins University Press; 1996.

57. Grasselli, M.; Pelinovsky, D. Numerical Mathematics. 1st ed.. Sudbury, MA: Jones and Bartlett Publishers; 2008.

58. MacQueen, JB. 5th Berkeley Symposium on Mathematical Statistics and Probability; University of California Press; Berkeley, CA. 1967. p. 281

59. Johnson, RA.; Wichern, DW. Applied multivariate statistical analysis. 5th ed.. Upper Saddle River, NJ: Pearson; 2002.

60. Newville M, Ravel B, Haskel D, Rehr JJ, Stern EA, Yacoby Y. Physica B. 1995:208–209. 154.

61. Newville, M. FEFFIT. Chicago, IL: http://cars.uchicago.edu/~newville/feffit/ [Last accessed January 2013]

62. Liu Y, Meirer F, Williams PA, Wang J, Andrews JC, Pianetta P. J. Synch. Rad. 2012; 19:281.

63. Lerotic M, Jacobsen C, Schäfer T, Vogt S. Ultramicroscopy. 2004; 100:35. [PubMed: 15219691]

64. Lu Z, Chen H, Robert R, Zhu BYX, Deng J, Wu L, Chung CY, Grey CP. Chem. Mater. 2011; 23:2848.

65. Malik R, Burch D, Bazant M, Ceder G. Nano Lett. 2010; 10:4123. [PubMed: 20795627]

66. Cogswell DA, Bazant MZ. ACS Nano. 2012; 6:2215. [PubMed: 22304943]

67. Tang M, Belak JF, Dorr MR. J. Phys. Chem. C. 2011; 115:4922.

68. Meethong N, Huang HYS, Speakman SA, Carter WC, Chiang YM. Adv. Funct. Mater. 2007; 17:1115.

69. Song HK, Lee KT, Kim MG, Nazar LF, Cho J. Adv. Funct. Mater. 2010; 20:3818.

70. Chon MJ, Sethuraman VA, McCormick A, Srinivasan V, Guduru PR. Phys. Rev. Lett. 2011:107.

71. Woodford WH, Carter WC, Chiang YM. Energy Env. Sci. 2012; 5:8014.

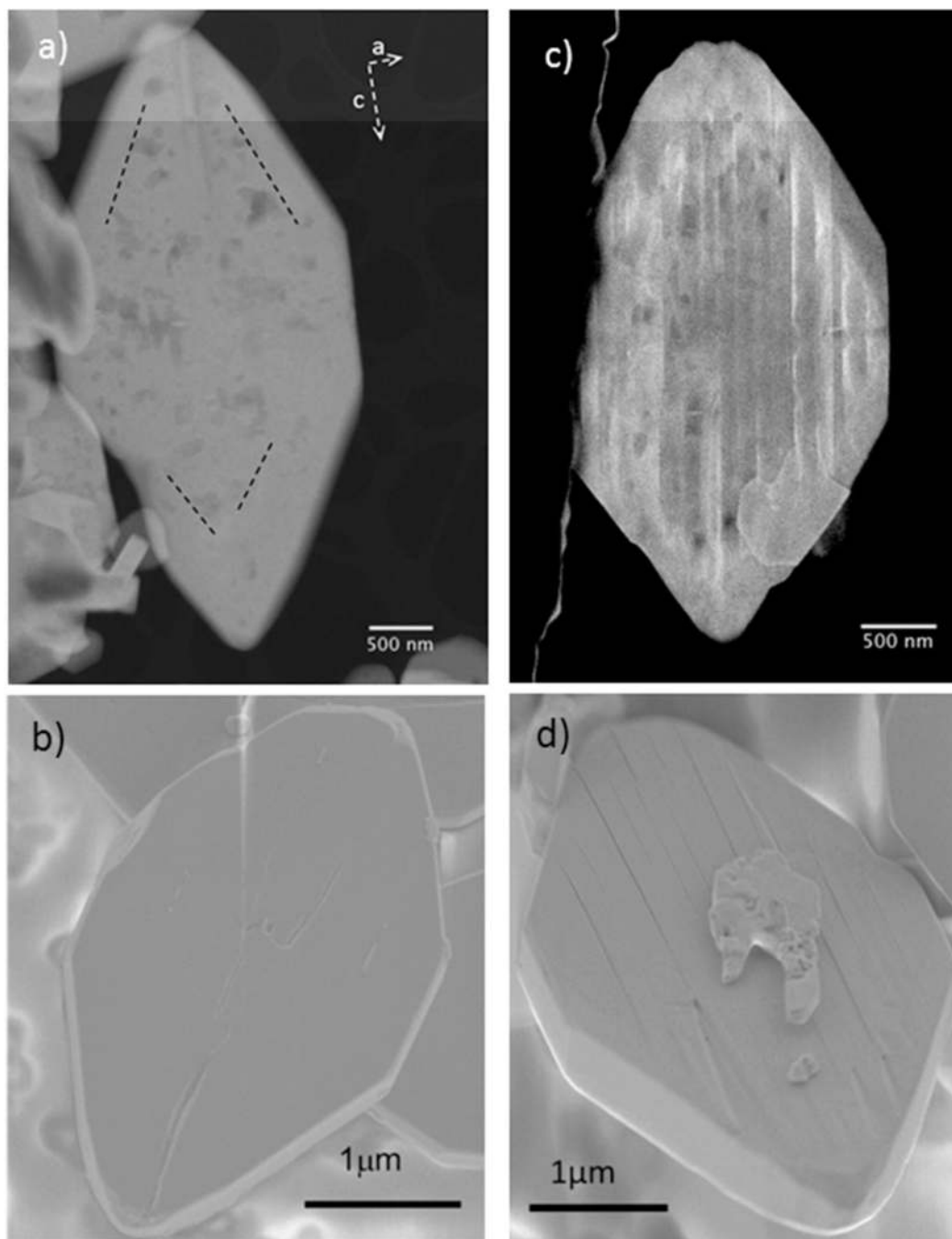72. Park J, Joo J, Kwon SG, Jang Y, Hyeon T. Angew. Chem. Int. Ed. 2007; 46:4630.

Figure 1.
Representative STEM HAADF images of pristine a) and c) of partially delithiated crystals in a sample with nominal composition $Li_{0.5}FePO_4$. The dashed line in a) is provided as a guide to the eye to differentiate regions of high and low defect density. Representative SEM images of b) pristine and d) delithiated Li_xFePO_4 crystals. The same batch of crystals was studied in both cases.
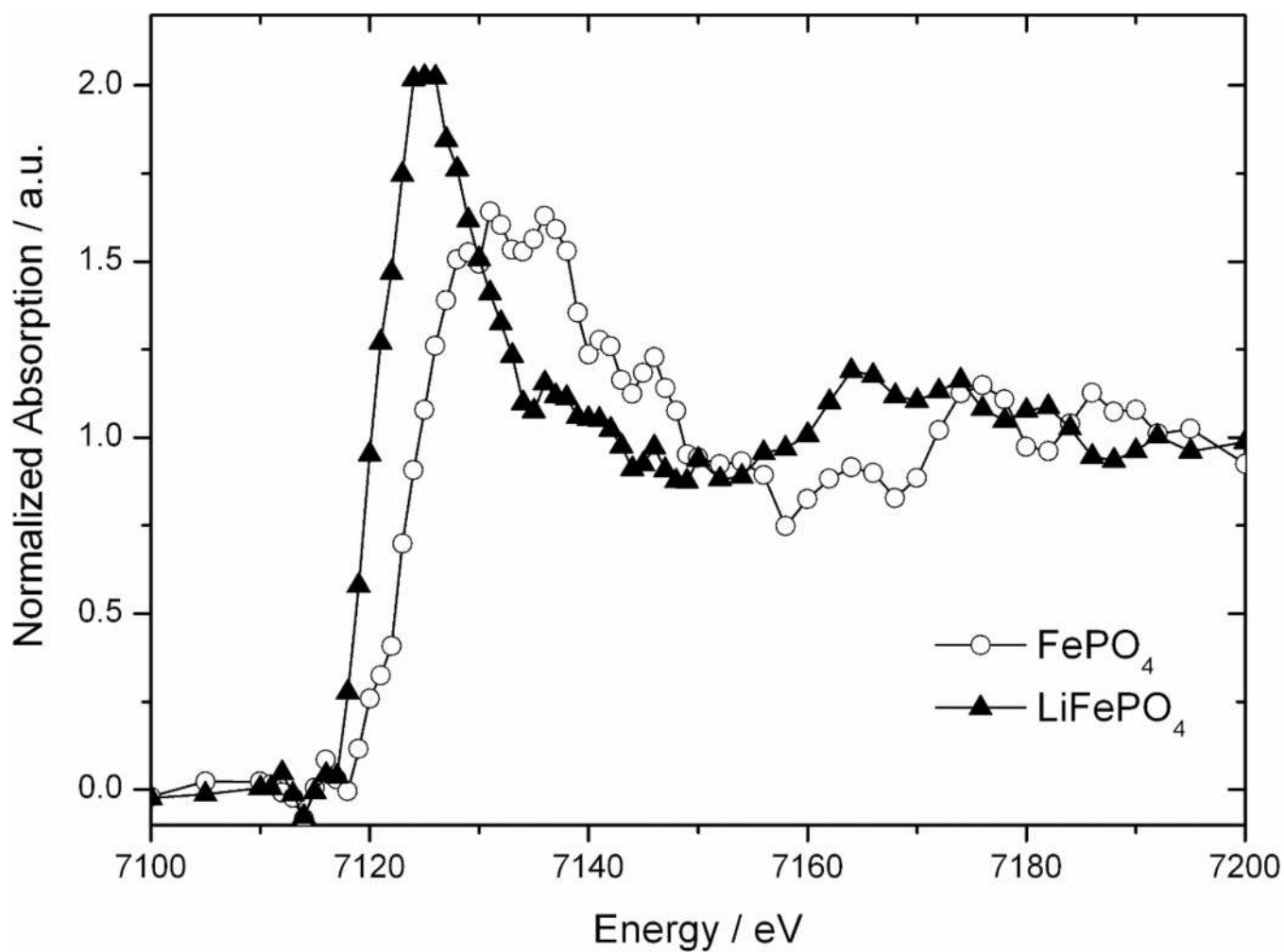
Figure 2.
Normalized absorption spectra of single-phase FePO$_4$ (open symbols) and LiFePO$_4$ (filled), collected by FF TXM, obtained by integrating the intensity of a full FOV containing multiple single-phase particles.
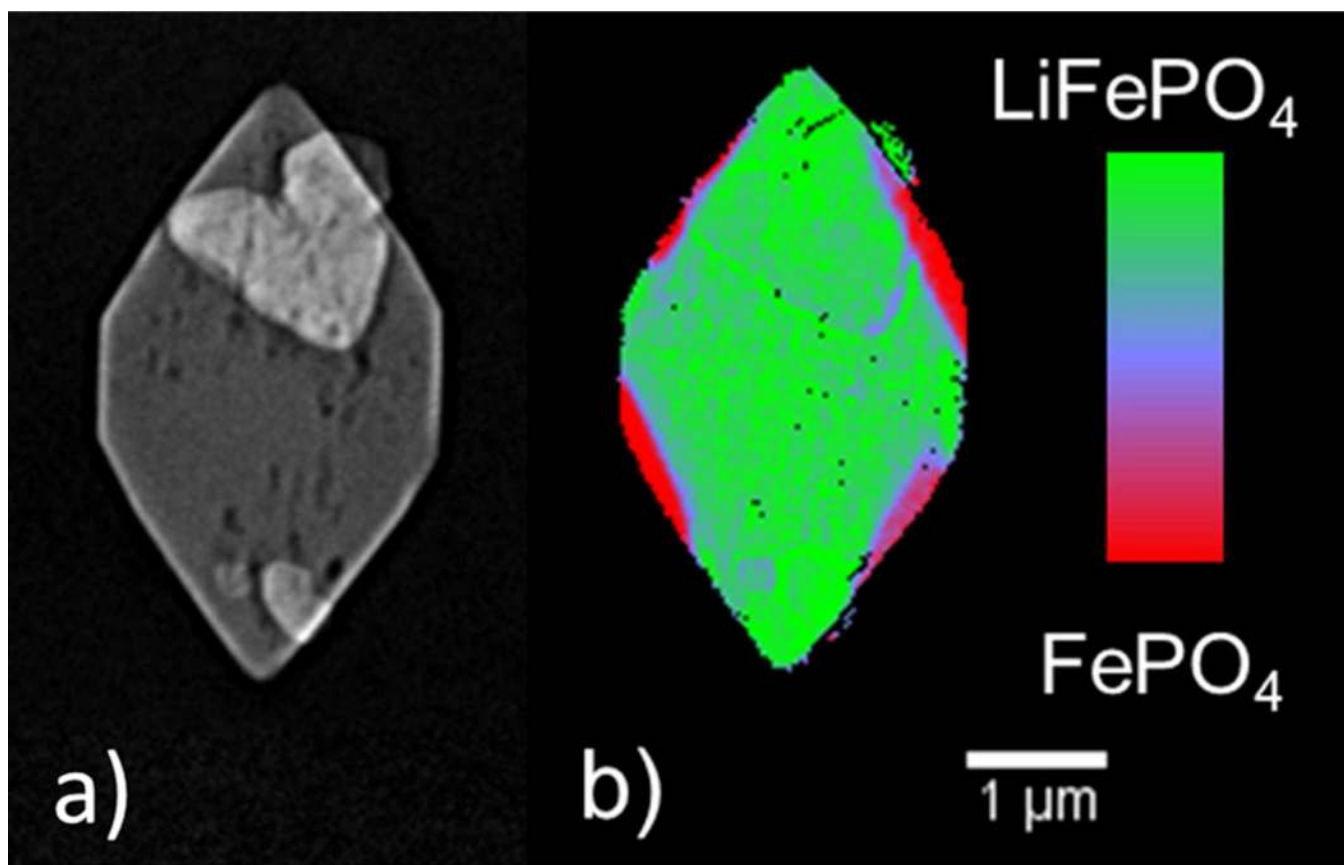
Figure 3.
a) FF TXM image of a selected crystal in a sample with nominal composition $Li_{0.74}FePO_4$ collected at 7080eV; b) chemical phase map obtained by LC fitting of XANES data at each pixel.
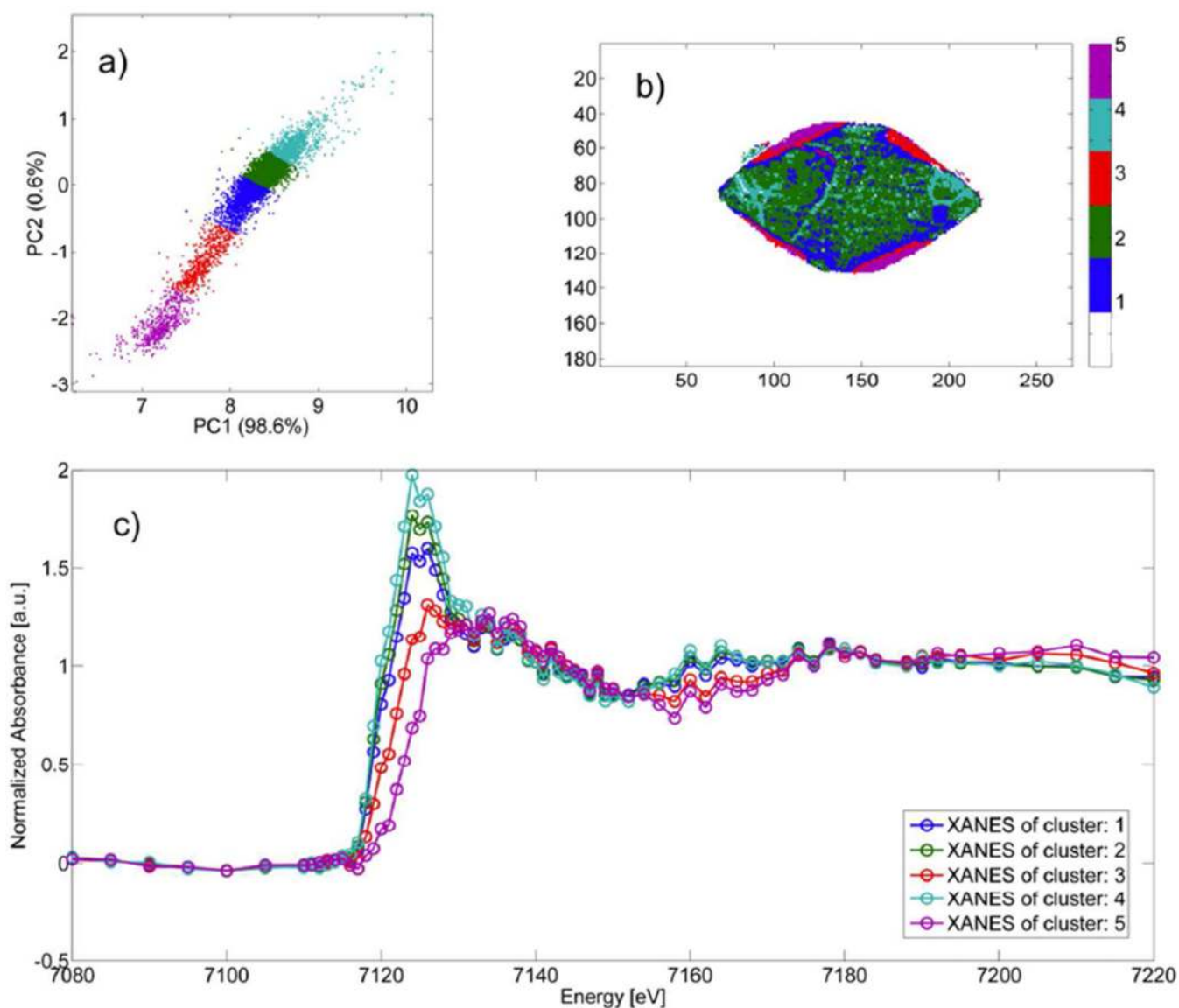
Figure 4.
Results of the k-means clustering in PC space performed for a selected crystal in a sample with nominal composition $Li_{0.74}FePO_4$. a) Score plot, i.e. pixels of the data set projected into 2 dimensional PC space (PC1 and PC2). Colors indicate the cluster to which each pixel has been assigned by the k-means algorithm. b) Cluster index image displaying the distribution of pixels assigned to each of the 5 clusters determined by k-means clustering. c) Average XANES of all pixels in each cluster, as indicated.
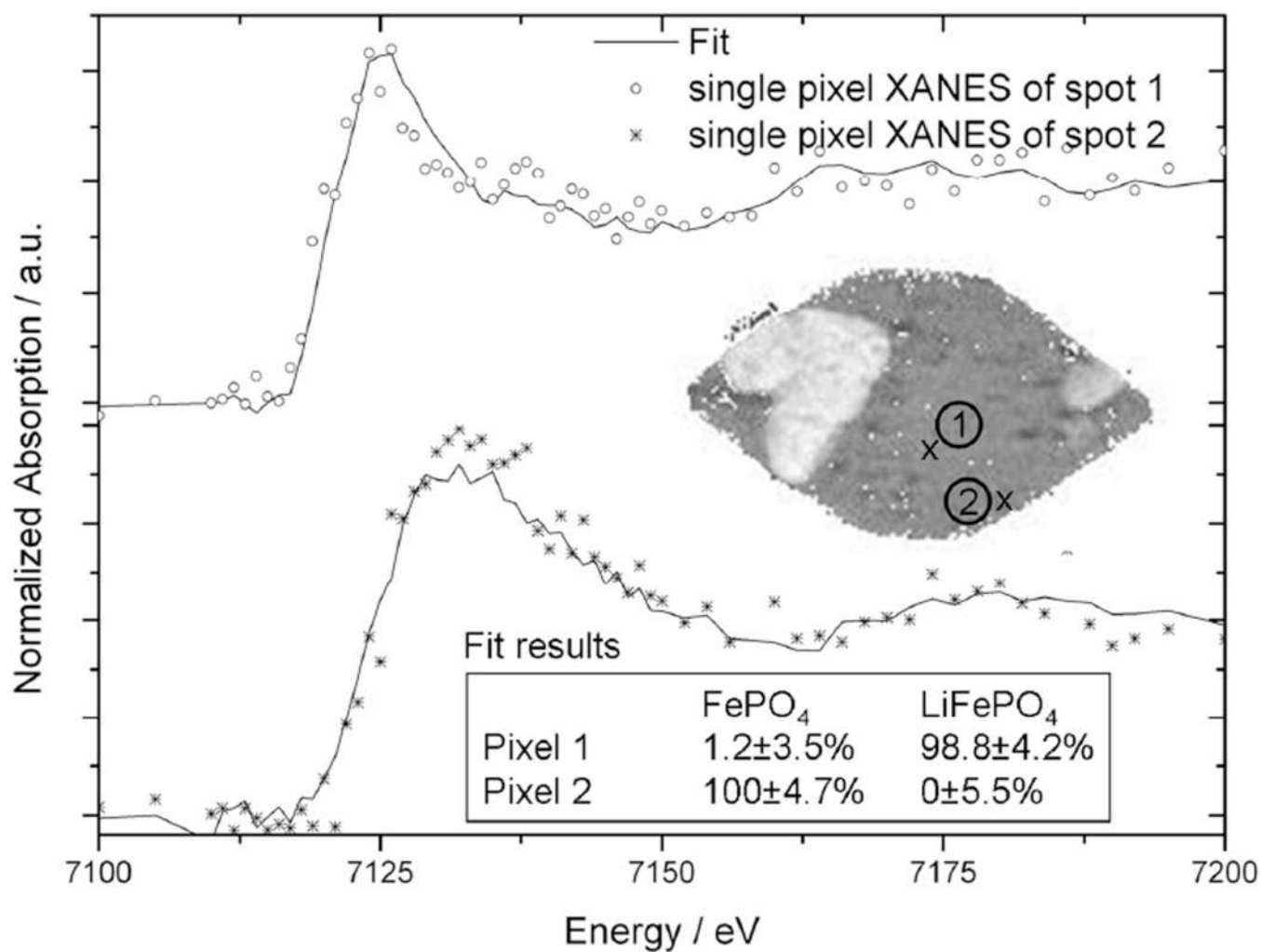
Figure 5.
Selected single pixel XANES, and results of LC fitting with $FePO_4$ and $LiFePO_4$ standards. Single pixels showing poor signal-to-noise ratios due to a low Fe concentration were filtered out by setting their intensity to 0 intensity at all energies.
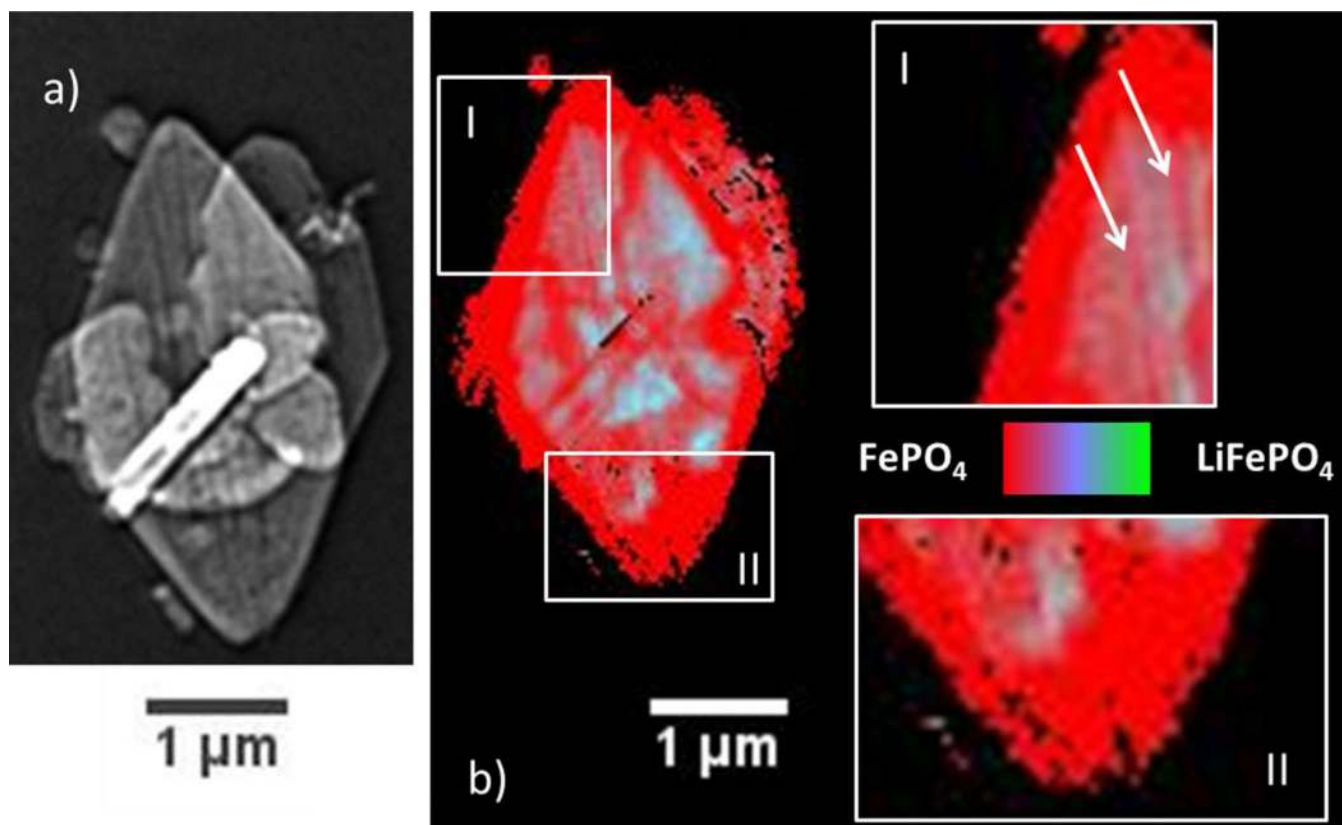
Figure 6.
a) FF TXM image of a selected crystal in a sample with nominal composition $Li_{0.5}FePO_4$ collected at 7220eV; b) chemical phase map obtained by LC fitting of XANES data at each pixel. Regions I and II are magnified by a factor of 2 from panel b. The white arrows point at an elongated domain with higher delithiation in the center of the crystal.
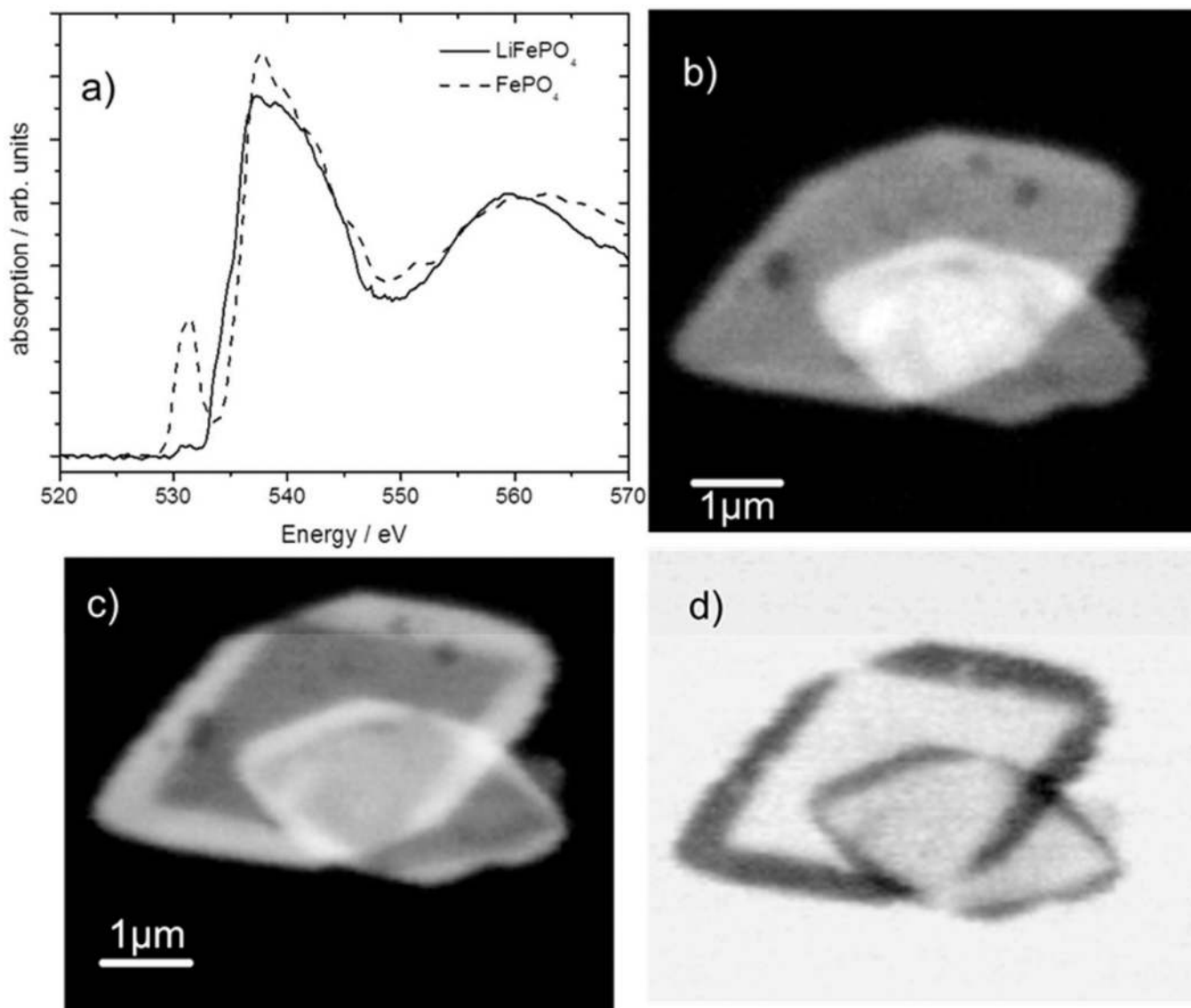
Figure 7.
a) O-K edge XAS of LiFePO$_4$ (solid) and FePO$_4$ (dashed) obtained from a line scan in STXM mode. STXM images of selected crystals in a sample with nominal composition Li$_{0.5}$FePO$_4$ collected at b) 528eV and c) 532.8eV; d) map of FePO$_4$ (dark areas) obtained by normalization of c) using b).